BBA - Bioenergetics 1860 (2019) 148058

Contents lists available at ScienceDirect

BBA - Bioenergetics

journal homepage: www.elsevier.com/locate/bbabio

Towards the competent conformation for catalysis in the ferredoxin-NADP$^+$ reductase from the *Brucella ovis* pathogen

Daniel Pérez-Amigot[a,b,1], Víctor Taleb[a,b,1], Sergio Boneta[b,c], Ernesto Anoz-Carbonell[a,b], María Sebastián[a,b], Adrián Velázquez-Campoy[a,b,d,e,f], Víctor Polo[b,c], Marta Martínez-Júlvez[a,b,*], Milagros Medina[a,b,*]

[a] Departamento de Bioquímica y Biología Molecular y Celular, Facultad de Ciencias, Universidad de Zaragoza, 50009 Zaragoza, Spain
[b] Instituto de Biocomputación y Física de Sistemas Complejos (Joint Units: BIFI-IQFR and GBsC-CSIC), Universidad de Zaragoza, 50018 Zaragoza, Spain
[c] Departamento de Química Física, Universidad de Zaragoza, 50009 Zaragoza, Spain
[d] Aragon Institute for Health Research (IIS-Aragon), Zaragoza 50009, Spain
[e] Biomedical Research Networking Center in Digestive and Hepatic Diseases (CIBERehd), Madrid, Spain
[f] Fundacion ARAID, Government of Aragon, Zaragoza 50018, Spain

ARTICLE INFO

Keywords:
Bacterial ferredoxin-NADP(H) reductase
Hydride transfer
Charge-transfer complex
Active site geometry
Stopped-flow
X-ray diffraction
Molecular dynamics

ABSTRACT

Brucella ovis encodes a bacterial subclass 1 ferredoxin-NADP(H) reductase (BoFPR) that, by similarity with other FPRs, is expected either to deliver electrons from NADPH to the redox-based metabolism and/or to oxidize NADPH to regulate the soxRS regulon that protects bacteria against oxidative damage. Such potential roles for the pathogen survival under infection conditions make of interest to understand and to act on the BoFPR mechanism. Here, we investigate the NADP$^+$/H interaction and NADPH oxidation by hydride transfer (HT) to BoFPR. Crystal structures of BoFPR in free and in complex with NADP$^+$ hardly differ. The latter shows binding of the NADP$^+$ adenosine moiety, while its redox-reactive nicotinamide protrudes towards the solvent. Nonetheless, pre-steady-state kinetics show formation of a charge-transfer complex (CTC-1) prior to the hydride transfer, as well as conversion of CTC-1 into a second charge-transfer complex (CTC-2) concomitantly with the HT event. Thus, during catalysis nicotinamide and flavin reacting rings stack. Kinetic data also identify the HT itself as the rate limiting step in the reduction of BoFPR by NADPH, as well as product release limiting the overall reaction. Using all-atom molecular dynamics simulations with a thermal effect approach we are able to visualise a potential transient catalytically competent interaction of the reacting rings. Simulations indicate that the architecture of the FAD folded conformation in BoFPR might be key in catalysis, pointing to its adenine as an element to orient the reactive atoms in conformations competent for HT.

1. Introduction

Plant-type ferredoxin-NADP$^+$ reductases are FAD-dependent enzymes structurally and functionally subdivided in two groups known as plastidic-type FNRs and bacterial-type FPRs [1,2]. The main function of FNRs in photosynthetic cells is the electron transfer from Photosystem I to NADP$^+$, via ferredoxin, to produce reducing power in the form of NADPH [2,3]. This reaction can be physiologically reversible and, thus, FNRs can also oxidize NADPH to provide reducing power to various metabolic processes in photosynthetic cells as well as in non-photosynthetic tissues and in some bacteria [4–6]. FPRs in general work in the NADPH oxidation sense of the reaction. In heterotrophic bacteria

Abbreviations: CHES, 2-(cyclohexylamino)ethanesulfonic acid; CTC, charge transfer complex; DCPIP, 2,6-diclorophenolindophenol; DMSO, dimethyl sulfoxide; *E. coli*, *Escherichia coli*; FAD, flavin adenine dinucleotide; FNR, plastidic type ferredoxin-NADP$^+$ reductase; FPR, bacterial type ferredoxin-NADP$^+$ reductase; HEPES, 4-(2-hydroxyethyl)-1-piperazineethanesulfonic acid; HT, hydride transfer; IPTG, isopropyl β-D-1-thiogalactopyranoside; ITC, isothermal titration calorimetry; MD, molecular dynamics; MES, 2-(N-morpholino)ethanesulfonic acid; NADP$^+$ and NADPH, oxidized and reduced forms of the nicotinamide adenine dinucleotide phosphate; PEG, polyethylene glycol; PIPES, piperazine-*N*,*N*′-bis(2-ethanesulfonic acid); ROS, reactive oxygen species; SDS-PAGE, sodium dodecyl sulfate polyacrylamide gel electrophoresis; Tris, tris(hydroxymethyl) aminomethane

* Corresponding authors at: Departamento de Bioquímica y Biología Molecular y Celular, Facultad de Ciencias, Universidad de Zaragoza, Pedro Cerbuna, 12, 50009 Zaragoza, Spain.
E-mail addresses: mmartine@unizar.es (M. Martínez-Júlvez), mmedina@unizar.es (M. Medina).
[1] These two authors have equally contributed to the study and must both be considered as first authors.

https://doi.org/10.1016/j.bbabio.2019.148058
Received 16 June 2019; Received in revised form 19 July 2019; Accepted 2 August 2019
Available online 05 August 2019
0005-2728/

they usually provide electrons, via ferredoxin or flavodoxin, to processes such as nitrogen, hydrogen, methane or CO_2 assimilation and fixation, activation of anaerobic enzymes, fatty acid desaturation or β-carotene hydroxylation [1,2]. A key antioxidant role in the protection of Gram negative bacteria against changing environments is also related to their NADPH oxidase activity [7–9]. Thus, FPRs are reported as a component of the soxRS regulon system that protects bacteria against superoxide and nitric oxide damage. In this context, at least five loci involved in the superoxide response of *Escherichia coli* are related to redox processes including the *fpr* gene, with NADPH formation and FPR protein levels stimulated when bacteria are exposed to oxidative environments [10–13]. Therefore, some bacteria finely regulate the NADP(H) pool homeostasis, and its deployment to the oxidized state, by the FPR action to produce the oxidation of the soxRS sensor. This later fact in turn activates the protective bacterial response under oxidative environments [14].

Both FNRs and FPRs fold in two domains, the N-terminal being the main responsible for FAD binding while the C-terminal domain binds $NADP^+$/H [1–3,9,15]. Despite overall FAD binding is similar, differences are found in its conformation that is respectively extended and folded. The extended FAD in FNRs is favoured by a *β*-hairpin structure that is replaced by a short loop in FPRs (Fig. SP1A). On its side, the folded FAD in FPRs is stabilised by the stacking of its adenosine to an aromatic residue found in a C-terminal tail present in FPRs but absent in FNRs. A key dissimilarity among FNRs and some FPRs also occurs at the active site. The isoalloxazine ring of FNRs stacks between two aromatic residues, being the one facing its *Re*-face a highly conserved C-terminal Tyr that controls substrates/products access/release as well as the optimal catalytic competent conformation for catalysis [2,16–18]. Subclass II FPRs conserve this aromatic residue, but subclass I members lack it (Fig. SP1A). Such traits are claimed as the causes for differences in catalytic efficiencies described between FNRs and FPRs.

The Gram negative α-proteobacterium *Brucella ovis* has a *fpr* gene (codifying for BoFPR) whose immediate downstream *sodr* gene codifies for a superoxide dismutase (SOD). SOD enzymes are directly involved in the process of reactive oxygen species (ROS) elimination, and its overexpression in some *Brucella* genus inhibits bacterial intracellular growth [19]. Noticeably, *sodr* genes are found immediately upstream of *fpr* in some highly related Rhizobiales (which share more than 80% of sequence identity). In most bacteria the *fpr* genomic context lacks *sodr* genes, but contains genes for ferredoxins and/or flavoproteins (Fig. SP1B). As chromosomal proximity in prokaryotes can relate to gene co-regulation [20], a functional association might be envisaged between BoFPR and BoSOD. Bacteria from the genus *Brucella* are facultative intracellular pathogens that cause brucellosis in humans and many animals, including cows, goats, sheep, dogs, and pigs. *B. ovis* is the causative agent of this zoonosis in sheep, causing genital injuries, placentitis, perinatal mortality increase and a lack of fertility [21–23]. The host tries to cope with the infection through phagocytosis involving the activation of neutrophils which undergo the respiratory burst releasing of ROS intended to target foreign pathogens [24]. Since in Gram negative bacteria FPR might perform an important function in ROS response, processes involving BoFPR might be of utmost importance for the survival of *B. ovis* under infection conditions.

Better understanding of the proteins that support *Brucella* intracellular growth is critical to design safe and effective vaccines and treatments of brucellosis. In this context, we present here the isolation of BoFPR, as well as a study of its mechanism for NADPH oxidation. Our combined spectroscopic, kinetic and structural (both experimental and theoretical) approaches provide an insight into the molecular mechanism for NADPH oxidation by BoFPR. In addition, we present structural details on the contribution of the FAD folded conformation and of the C-terminal tail of FPRs to the formation of a geometry that allocates the N5 of the isoalloxazine of FAD and the C4 of the nicotinamide from NADPH in close proximity. We consider that knowledge about these facts in the context of what is known about other members of this family is of interest both from the mechanistic point of view in FPRs and to consider BoFPR a potential therapeutic target.

2. Materials and methods

2.1. Protein production

The BOV-0348 gene of *B. ovis* ATCC 25840 was synthetized and cloned into the *Nco*I/BamHI sites of the pET-28a(+) plasmid by GenScript. In this way the codifying fragment contains the BoFPR gene preceded by an extension coding for a His_6-Tag plus a PreScission protease cleavage sequence. PET28a-BoFPR was used to transform *E. coli* BL21 (DE3) competent cells. Transformed cells were selected on LB/agar with 30 μg/mL kanamycin and then grown in LB media. BoFPR expression was induced by overnight incubation with 200 μM IPTG at 37 °C. Cells were harvested by centrifugation and stored at −20 °C. To purify BoFPR, cells were thawed, resuspended in cell disruption buffer (20 mM potassium phosphate, pH 7.4, 10 mM imidazole, 0.5 M NaCl, and 1 μM phenylmethanesulfonyl fluoride) and broken by ultrasonic treatment at 4 °C (12 cycles of 30 s) in a DRH UP200 DR sonicator (Hielscher). The cell debris was removed by centrifugation and the supernatant was loaded onto a His-Trap HP column (GE Healthcare) equilibrated with cell disruption buffer. The column was washed with the same buffer. His_6-BoFPR was then eluted by using a 10 → 500 mM imidazole gradient and collected in aliquots while recording absorbance at 280 nm. Fractions being yellow were analysed by SDS-PAGE. Those containing BoFPR were pooled and dialysed against 25 mM Tris/HCl, pH 7.4. To remove the His_6-Tag, the protein was incubated with the PreScission Protease and then loaded in tandem His-Trap and GST-Trap columns (GE Healthcare) to eliminate both the His_6-tag and the protease. Purification was completed using a HiPrep™ 26/60 Sephacryl® S-200 HR chromatography (GE Healthcare). Pure BoFPR fractions were pooled and stored at −20 °C.

2.2. Spectroscopic analyses

UV–visible absorption spectra were recorded in an UV–Vis Cary 100 spectrophotometer (Agilent Technologies) at 25 °C. CD spectra were obtained in a Chirascan spectropolarimeter (Applied Photophysics Ltd.) at 25 °C with 5 μM protein for the far-UV region and 20 μM for the near-UV and visible regions, with 0.1 and 1 cm path length cuvettes, respectively. Fluorescence spectra were monitored using a Cary Eclipse fluorimeter (Agilent Technologies) with 20 μM protein solutions. The molar absorption coefficient for BoFPR at 451 nm was spectrophotometrically determined by thermal denaturation of the protein for 10 min at 90 °C, followed by centrifugation, separation of the precipitated apoprotein, and spectroscopic quantification of the FAD released to the supernatant as previously described [25]. Spectral evolution upon stepwise reduction of BoFPR (20 μM) was achieved by photoreduction in the presence of 5-diazariboflavin (4 μM) and 3 mM EDTA under anaerobic conditions [26]. Unless otherwise stated samples were in 25 mM Tris/HCl, pH 7.4.

2.3. Isothermal titration calorimetry

Interaction of $BoFPR_{ox}$ with $NADP^+$ was evaluated by isothermal titration calorimetry (ITC) using a high precision Auto-ITC200 calorimeter (MicroCal-Malvern Panalytical) thermostated at 25 °C. Interaction parameters were obtained by direct titration of $BoFPR_{ox}$ (10 μM in the cell) with $NADP^+$ solutions (150 or 250 μM in the syringe) in 25 mM Tris/HCl, pH 7.4, following procedures described previously [27,28]. A home-derived model for one binding site implemented in Origin 7.0 (OriginLab) was used to determine the binding stoichiometry (N), the association constant (K_a), and the binding enthalpy (ΔH) [27,28]. The values of the dissociation constant (K_d), the free energy of binding (ΔG) and the enthalpic contribution to the

binding ($-T{\cdot}\Delta S$) were derived from basic thermodynamic relationships.

2.4. Evaluation of BoFPR thermal stability

The increase in the FAD cofactor fluorescence by its dissociation from the holoprotein upon thermal unfolding was used to evaluate BoFPR stability through assessing the midpoint temperature for flavin release (T_{mFAD}). Denaturation curves were recorded in 25 mM Tris/HCl, pH 7.4, using a Varian Cary Eclipse fluorimeter (Agilent Technologies Ltd.) from 20 to 85 °C with scan rates of 1.5 °C/min and 2 μM protein, both in the absence and presence of a 50-fold excess of $NADP^+$. Samples were excited at 450 nm and fluorescence was recorded at 530 nm. T_{mFAD} values were determined by analysing thermal FAD release curves as one-transition (i.e., a two-state process, native ↔ unfolded or FAD bound ↔ unbound, N ↔ U) by applying the following equations [29]:

$$S_{obs} = \frac{S_N + S_U e^{-(\Delta G/RT)}}{1 + e^{-(\Delta G/RT)}} = \frac{S_{N,0} + m_N T + (S_{U,0} + m_U T) e^{-(\Delta G/RT)}}{1 + e^{-(\Delta G/RT)}} \quad (1)$$

where S_{obs} is the measured protein signal at a given temperature (T), S_N and S_U are the intrinsic fluorescent signals corresponding to protein-bound FAD and protein-free FAD, respectively, and considered linear functions of the temperature ($S_{N,0}$ and $S_{U,0}$ are the y-axis intercepts, and m_N and m_U are the slopes). On the other hand, the free energy difference in Eq. (1) follows, $\Delta G_i = \Delta H_i\left(1 - \frac{1}{T_{mFADi}}\right) + \Delta C_{Pi}\left(T - T_{mFADi} - T\ln\frac{T}{T_{mFADi}}\right)$, where ΔH_i is the van't Hoff enthalpy for each FAD release transition, T_{mFADi} is the mid-transition temperature for FAD release, ΔC_{Pi} is the heat capacity change for the unfolding transition associated with FAD release, and R is the ideal gas constant.

The heat capacity of $BoFPR_{ox}$ and $BoFPR_{ox}$:$NADP^+$ samples was measured as a function of temperature ($\Delta C_P(T)$) using a High-sensitivity differential scanning PEAQ-DSC automated microcalorimeter (MicroCal-Malvern Panalytical). Thermal denaturation scans were performed with 20 μM degassed $BoFPR_{ox}$ solutions, both in the absence and presence of a 5-fold excess of $NADP^+$ at a scanning rate of 1 °C/min from 10 to 95 °C. Reference solutions (containing buffers but lacking BoFPR and $NADP^+$) were treated similarly to record the baseline of the instrument before experiments. No precipitation/aggregation occurred during thermal denaturation. Thermograms were baseline-corrected and analysed using a home-derived routine implemented in Origin 7 (OriginLab).

2.5. Steady-state enzymatic assays and evaluation of the inhibitory effects

The BoFPR NADPH-dependent diaphorase activity was determined by following the 2,6-diclorophenolindophenol (DCPIP) reduction (95 μM) at 620 nm (ε_{620} = 21 mM^{-1} cm^{-1}) in samples containing 20 nM BoFPR and a 0–50 μM NADPH range [30]. Kinetic measurements were carried out at 25 °C, in 25 mM Tris/HCl, pH 7.4. k_{cat} and K_m^{NADPH} values were calculated by data fitting to the Michaelis-Menten equation considering inhibition by excess of NADPH,

$$\frac{v}{[BoFPR]} = \frac{k_{cat}[NADPH]}{K_m^{NADPH} + [S](1 + [S]/K_i)} \quad (2)$$

which also provided the corresponding inhibition constant, K_i. NADPH consumption when using oxygen and superoxide as potential BoFPR electron acceptors was quantified by monitoring the decrease in absorbance at 340 nm. Superoxide was added as a potassium 18-crown-6 salt (Sigma-Aldrich) dissolved in dimethyl sulfoxide (DMSO).

The diaphorase activity was also assayed at different pH values using as buffers 25 mM MES in the pH 5.5–6.0 range, 25 mM PIPES in the pH 6.3–6.7 range, 25 mM Tris/HCl in the pH 7.0–8.4 range, and 25 mM CHES in the pH 8.7–9.2 range, all of them containing 150 mM NaCl. The relative activities obtained were fitted to a three-state model using the following equation:

$$F = \frac{F_A + F_N 10^{a} + F_B 10^{(a+b)}}{1 + 10^{a} + 10^{(a+b)}} \quad (3)$$

where F_A, F_N and F_B are the activities (%) at acidic, neutral and basic pH values respectively, and $a = m(\text{pH} - \text{p}K_{a1})$ and $b = n(\text{pH} - \text{p}K_{a2})$, being m and n the number of protons exchanged in each of the two transitions [31].

The inhibitory effect of small molecules (Table SP1) on the BoFPR diaphorase activity was evaluated, in 25 mM Tris/HCl, 2% DMSO, pH 7.4, at 25 °C, using 20 nM BoFPR, saturating DCPIP (95 μM) and NADPH (50 μM), and varying the concentration of the compounds. These data were used to determine the concentration of the compound causing 50% enzyme inhibition (IC_{50}) and maximal inhibition (IC_{max}), as well as the BoFPR residual activity at IC_{max} [30].

2.6. Stopped-flow kinetic measurements

Fast reduction of $BoFPR_{ox}$ by NADPH was evaluated by using a SX.18MV stopped-flow spectrophotometer (Applied Photophysics Ltd.) with a photodiode array detector following settled down procedures [32]. All samples were made anaerobic before introduction into the stopped-flow syringes. BoFPR (~20 μM) was mixed with a range of NADPH concentrations at ratios from 1:1 to 1:20 in 25 mM Tris/HCl, pH 7.4 at both 6 and 25 °C. Multiple wavelength absorption data (400–1000 nm) were collected and processed using the X-Scan software (Applied Photophysics Ltd.). Time spectral deconvolution was performed by global analysis and numerical integration methods using Pro-Kineticist (Applied Photophysics Ltd.). Collected data were fitted to either single (A → B or B → C) or two (A → B → C) steps model allowing estimation of the corresponding observed conversion rate constants ($k_{A\to B}$, $k_{B\to C}$) at each NADPH concentration, as well as obtaining spectral information of intermediate and final species [32,33]. A, B and C are spectral species, reflecting a distribution of enzyme intermediates (reactants, charge-transfer complexes (CTCs), products, Michaelis complex) at any certain time along the course of the enzyme:coenzyme interaction and HT or reorganization processes and do not necessarily represent a single distinct enzyme intermediate. Moreover, none of them represents individual species and, their spectra cannot be included as fixed in the global-fitting. $k_{A\to B}$ or $k_{B\to C}$ showing hyperbolic dependence profiles on the NADPH concentration was fitted to the equation describing binding at a single site followed by reorganization processes or a HT, allowing determination of the corresponding interaction constant (K_d) as well as rate constants for the subsequent process (k) [33].

$$k_{obs} = k_{A\to B} = k_{B\to C} = \frac{k{\cdot}[NADPH]}{[NADPH] + K_d} \quad (4)$$

where, depending on $k_{A\to B}$ or $k_{B\to C}$ processes, k might respectively account for the kinetic limiting rate for BoFPR:NADPH complex formation, k_{on}, or for the HT rate constant, k_{HT}; while K_d might respectively account for the BoFPR:NADPH complex dissociation constant, K_d^{NADPH}, or for a reorganization constant related to the transformation between reaction intermediate species, K_d^{reg}.

2.7. Protein crystallization and X-ray diffraction

Crystals of BoFPR, alone and complexed with $NADP^+$, were obtained using either the hanging-drop or sitting-drop vapour-diffusion methods at 291 K. A typical drop consisted of 0.33 μl of BoFPR (9.5 mg/ml) in Tris/HCl 25 mM, NaCl 150 mM, pH 7.4 and 0.33 μl of reservoir solution, set up by a NANODROP II (Innovadyne Technologies, Inc. USA). Drops were equilibrated against 60 μl of reservoir solution. Adequate crystals for X-ray diffraction were obtained in the condition 25% PEG 4 K, 0.1 M MES, pH 6.5 and 0.2 mM $MgCl_2$ (C7 of Classic screen from Jena Bioscience). Crystals reached maximum size in one week and were cryoprotected with 20% of glycerol before diffraction.

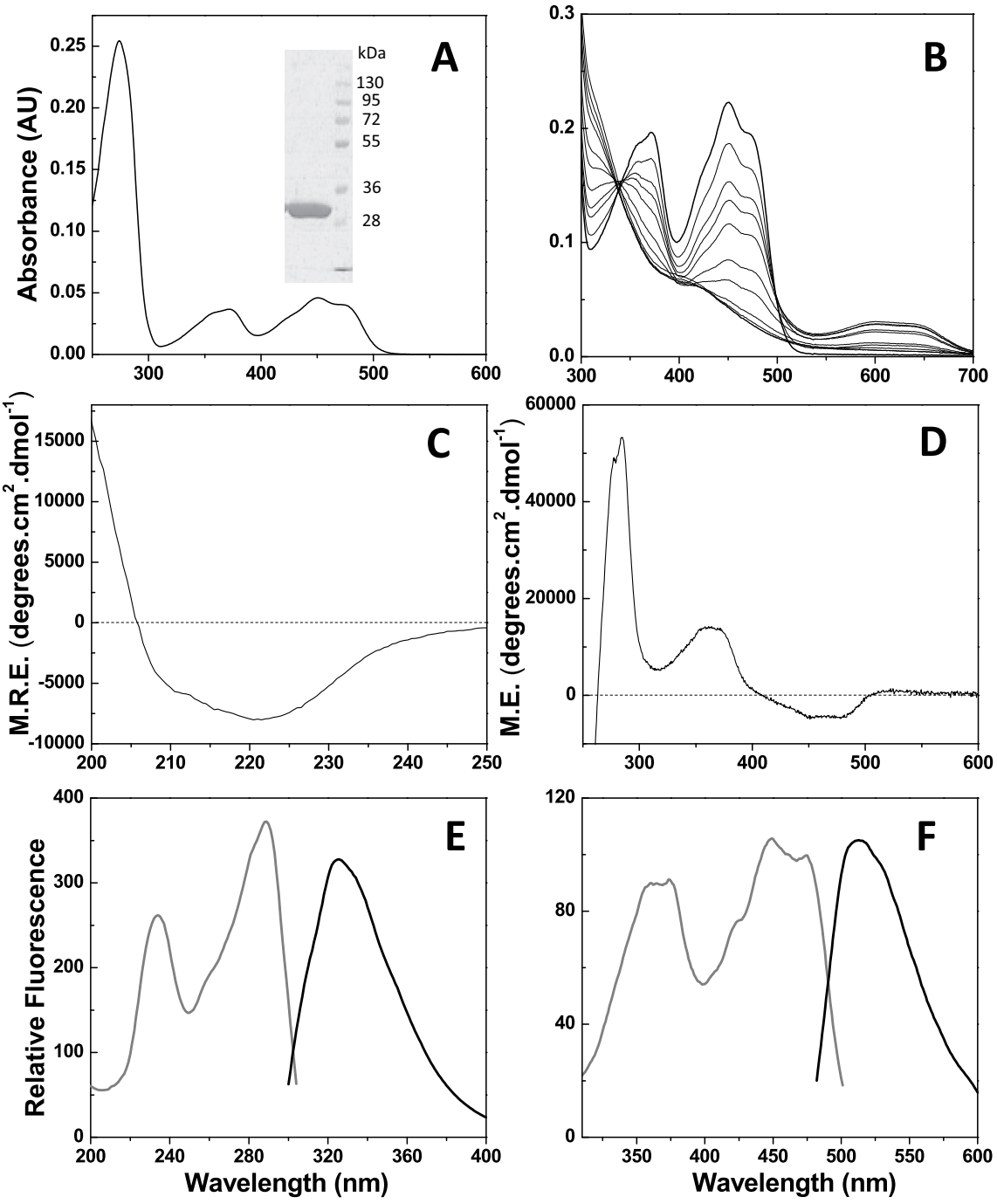

Fig. 1. Spectroscopic properties of BoFPR. (A) UV/Vis absorption spectrum of BoFPR (4 μM). The inset shows the SDS-PAGE of the purified sample (lane 1) and of several Molecular Weight Markers (lane 2). (B) Spectra evolution for the photoreduction of BoFPR (20 μM) under anaerobic conditions and in the presence of 4 μM 5-deazariboflavin and 3 mM EDTA. (C) far-UV and (D) near-UV/Vis CD spectra of BoFPR. Spectra obtained with 5 μM (0.1 cm path-length cuvette) and 20 μM (1 cm path-length cuvette) protein respectively. (E) Far UV and (F) visible fluorescence spectra of BoFPR (20 μM). Black lines show the fluorescence emission spectra when exciting at 280 (E) and 450 (F) nm, whereas grey lines correspond to excitation spectra when collecting fluorescence at 326 (E) and 514 (F) nm. All spectra were recorded in Tris/HCl 25 mM, pH 7.4 at 25 °C.

Crystals of $BoFPR_{ox}$:$NADP^+$ complex were obtained adding $NADP^+$ in powder on drops containing crystals of BoFPR, previously grown in 2% PEG 400, 0.1 M HEPES, pH 7.5 and 2 M ammonium sulfate, and incubating that mixture for 25 min. Crystals were cryoprotected with a solution containing 85% of mother liquor and 15% of glycerol with 10 mM $NADP^+$. Data were collected from a single crystal of $BoFPR_{ox}$ using the synchrotron source DLS beamline I24 and a Pilatus3 6 M detector with a wavelength of 0.968620 Å, to a maximum resolution of 1.69 Å. Crystals belonged to $P4_1$ tetragonal space group with one molecule in the asymmetric unit and unit cell dimensions shown in Table SP2. $BoFPR_{ox}$:$NADP^+$ diffraction data were collected in the B13 (XALOC) beamline at ALBA synchrotron with a Dectris Pilatus 6M detector and a wavelength of 0.979260 Å, to a maximum resolution of 1.4 Å. Crystals belonged to the $P2_12_12_1$ group (Table SP2). All data sets were processed, scaled and reduced with XDS [34] and SCALA [35] from the CCP4 package [36]. The structures were solved by molecular replacement using the MOLREP [37] program from CCP4 [36] and the structure of *P. aeruginosa* FPR (PDB ID: 2QDX) as search model.

Automatic refinement was performed by Refmac5 [38] from the CCP4 package and alternating manual model building by WinCOOT [39]. Final models compromised residues 2–258 and one FAD for both structures and 166 and 257 water molecules for $BoFPR_{ox}$ and $BoFPR_{ox}$:$NADP^+$, respectively. Additionally, one SO_4^{2-} and one $NADP^+$ molecules were refined in the complex structure. PROCHECK [40] was used to assess the final structure quality. Relevant data collection statistics and refinement parameters are presented in Table SP2. The coordinates and structure factors for $BoFPR_{ox}$ and $BoFPR_{ox}$:$NADP^+$ have been deposited in the Protein Data Bank with PDB IDs 6RR3 and 6RRA, respectively.

2.8. Molecular dynamics simulations

An initial model of $BoFPR_{ox}$, including the FAD cofactor, was built using the *A. vinelandii* FPR crystallographic structure (PDB ID: 1A8P) [41] as template and Prime [42,43] after a Needleman-Wunsch sequence alignment (zhanglab.ccmb.med.umich.edu/NW-align). Protonation states were adjusted to pH 7.0. To produce a $BoFPR_{ox}$:NADPH complex model, the NADPH coenzyme was manually introduced in the $BoFPR_{ox}$ model and allocated using as models the BoFPR:$NADP^+$ (PDB ID: 6RRA) and *P. aeruginosa* FPR:$NADP^+$ (PDB ID: 3CRZ) complexes [44]. PyMOL was used for structural manipulations and figures production [45]. All-atom molecular dynamics (MD) simulations were performed using GROMACS 5.1.5 [46]. AMBER ff03 [47] parameters were applied to the amino acids while ligands were parameterised using GAFF [48] and density functional theory (DFT). Atomic charges were calculated with the Gaussian09 package [49] at the B3LYP/6-31G level of theory and used with Antechamber [50] through ACPYPE [51]. Oxidized FAD and NADPH redox states for the cofactor and coenzyme have been used respectively in all simulations. Each system was placed in the centre of a rhombic dodecahedron box, solvated with a TIP3P water model and neutralised by adding sodium ions. Final systems consisted in 37,456 and 37,410 total atoms for $BoFPR_{ox}$ and $BoFPR_{ox}$:NADPH, respectively. A steepest descent minimization was performed to avoid close contacts or clashes. Desired conditions were achieved after a 100 ps simulation with NVT ensemble and the generation of random initial velocities, and a 100 ps simulation with NPT ensemble, both restraining the movement of atoms of protein and ligands with a 1000 $kJ{\cdot}mol^{-1}{\cdot}nm^{-1}$ harmonic potential. Longer NPT simulations with positions unrestrained were then performed, collecting the data every 10 ps. A time step of 2 fs and leap-frog integrator, periodic boundary conditions, Particle Mesh Ewald method for long range electrostatic interaction, Parrinello-Rahman method for pressure control, modified Berendsen method for temperature equilibration and LINCS to restrain bonds including hydrogen atoms were used. Trajectories were analysed using VMD [52] and GROMACS package tools [46]. *PROPKA* software was used to assign pK_a values to X-ray and model structures [53].

3. Results and discussion

3.1. BoFPR has the typical spectroscopic features of a member of the plant FNR family

After purification BoFPR shows a single band in SDS-PAGE that corresponds to a molecular weight of ~30 kDa, as well as an absorption spectrum with maxima at 274, 371 and 451 nm and a shoulder at 490 nm, with Abs_{274}/Abs_{451} ratio of 5.5 (Fig. 1A). Thermal denaturation confirms that BoFPR has FAD as cofactor, allowing also to determine a molar extinction coefficient of 11.5 ± 0.4 $mM^{-1}\,cm^{-1}$ at 451 nm in 25 mM Tris/HCl, pH 7.4. Upon stepwise photoreduction the BoFPR spectrum shows absorption decrease at 450 nm concomitant with the initial appearance of a new band with a maximum at 584 nm and its subsequent bleaching (Fig. 1B). Such spectral observations relate to transformation of the oxidized (ox) FAD state to the fully reduced state (hq) through the transient stabilisation of a neutral semiquinone (sq) state. Isosbestic points are detected at 340 nm and 260 nm for the ox/hq transition, and at 500 nm for the ox/sq transition. Nonetheless, maximal sq stabilisation is estimated below 25%, suggesting a lower midpoint reduction potential for the ox/sq one-electron transfer step, $E_{ox/sq}$, than for the sq/hq one-electron step. This later trait is typical in FNR family members that need to exchange electrons between obligatory two-electron transfer substrates, such as pyridine nucleotides, and obligatory one-electron transfer redox centres, such as iron-sulfur clusters [54].

The BoFPR far-UV CD spectrum has minima at 221.5 and at 208 nm (Fig. 1C), suggestive of folding in α-helixes and β-sheets. The 277.5 nm maximum in the near-UV CD suggests at least one Tryptophan internalized within the folded protein, while the Vis CD features relate to the FAD (maximum at 358 nm and minima at 451 and 478.5 nm) (Fig. 1D). When excited in the near-UV (280 nm) BoFPR emission is centred at 326 nm (Fig. 1E), suggestive of at least one tryptophan in a folded protein environment. In agreement, the corresponding excitation spectrum (Fig. 1E) has a maximum at 290 nm. The BoFPR Vis emission spectrum shows typical features of a strongly quenched flavin, in agreement with its excitation and absorption spectra (Fig. 1F and A). Altogether these data indicate that the purified BoFPR is correctly folded and contains one molecule of FAD per molecule of protein.

3.2. BoFPR binds the $NADP^+$/H and exhibits NADPH oxidoreductase activity

To evaluate the $BoFPR_{ox}$ ability to bind the expected product of its catalytic reaction, $NADP^+$, we first used differential spectroscopy in the flavin absorption region. Nonetheless, $NADP^+$ addition induces no spectral changes, suggesting that either $NADP^+$ does not bind to $BoFPR_{ox}$ or its binding does not affect the isoalloxazine electronic properties. Such behaviour differs from that reported for other FPRs and FNRs, where characteristic and species specific difference spectra have been reported [55,56]. The profiles for thermal release of the FAD from $BoFPR_{ox}$ also show that the presence of $NADP^+$ hardly affects T_{mFAD} ($T_{mFAD}^{BoFPRox}$ = 328.3 ± 0.3 K, $T_{mFAD}^{BoFPRox:NADP+}$ = 328.9 ± 0.3 K) and the related unfolding enthalpy ($\Delta H^{BoFPRox}$ = 100 ± 5 kcal/mol, $\Delta H^{BoFPRox:NADP+}$ = 120 ± 5 kcal/mol) (Fig. 2A). Similarly, DSC shows two partially overlapping transitions of similar temperatures ($T_{m1}^{BoFPRox}$ = 326.4 ± 0.5 K, $T_{m2}^{BoFPRox}$ = 328.6 ± 0.5 K, $T_{m1}^{BoFPRox:NADP+}$ = 326.3 ± 0.5 K, and $T_{m2}^{BoFPRox:NADP+}$ = 328.6 ± 0.5 K) and unfolding enthalpies ($\Delta H_1^{BoFPRox}$ = 138 ± 2 kcal/mol, $\Delta H_2^{BoFPRox}$ = 70 ± 3 kcal/mol, $\Delta H_1^{BoFPRox:NADP+}$ = 140 ± 2 kcal/mol and $\Delta H_2^{BoFPRox:NADP+}$ = 62 ± 2 kcal/mol) for $BoFPR_{ox}$ and $BoFPR_{ox}$:$NADP^+$ complex (Fig. 2B). Thus, $NADP^+$ does not induce BoFPR thermal stabilisation, contrary to that found in other FNRs [57]. Moreover, these analyses suggest that the $BoFPR_{ox}$ unfolding process of the FAD-binding and $NADP^+$-binding domains are not fully cooperative, with the FAD domain being just slightly more stable, and the presence of $NADP^+$ not having impact on the thermal stability of $BoFPR_{ox}$.

To further evaluate $NADP^+$ binding to $BoFPR_{ox}$ we used ITC. Fig. 2C provides a thermogram consistent with binding of a molecule per $BoFPR_{ox}$ molecule with $K_d^{BoFPRox:NADP+}$ = 3.7 ± 0.2 μM, ΔG = −7.4 ± 0.3 kcal/mol, ΔH = −32 ± 1 kcal/mol, and −T·ΔS = 24.6 kcal/mol. Therefore, $NADP^+$ binding to $BoFPR_{ox}$ under our experimental conditions is apparently enthalpically driven with an opposing entropic contribution. Binding affinity is in the range of plastidic FNRs, but changes are observed when comparing the enthalpic/entropic contributions ratio to the binding [27,28,57,58]. Altogether these data show that despite $BoFPR_{ox}$ is able to bind its $NADP^+$ product, the binding mode might differ from other family members. Thus, despite binding of the $NADP^+$ to $BoFPR_{ox}$ occurs, the nicotinamide moiety of the $NADP^+$ hardly influences the flavin environment and the protein thermal stability.

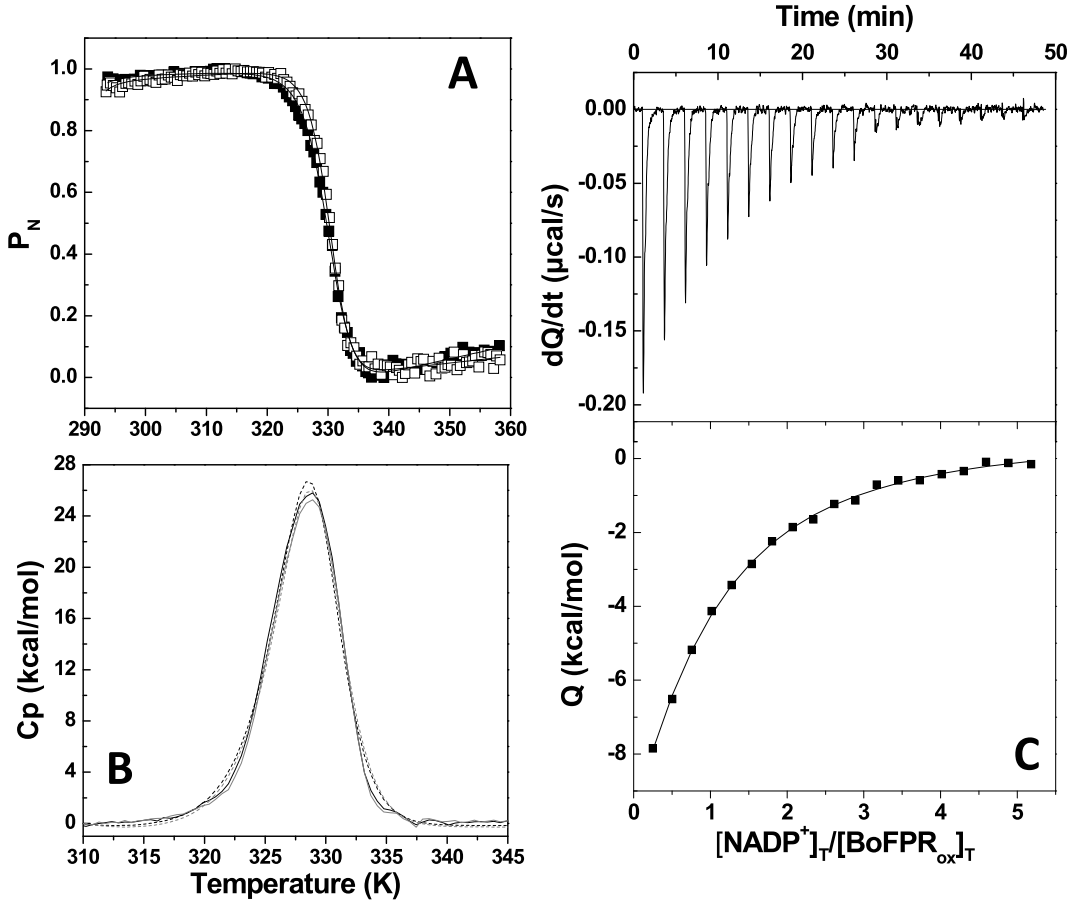

Fig. 2. The interaction of BoFPR with $NADP^+$. (A) Thermal denaturation curves of $BoFPR_{ox}$ (2 µM, closed squares) and $BoFPR_{ox}$:$NADP^+$ (2 µM:100 µM, open squares) roughly normalized to the fluorescence of the FAD bound fraction (P_N, from 1 to 0), with their global fits to a one-transition model represented by continuous lines. Decrease in FAD bound fraction was experimentally followed by increase in the FAD fluorescence upon its release from the holoprotein along a 20 to 85 °C temperature ramp. (B) DSC thermogram for solutions of $BoFPR_{ox}$ (20 µM, black) and $BoFPR_{ox}$:$NADP^+$ complex (20 µM:100 µM, grey). Fittings to a two-transition unfolding process are shown in dashed lines. (C) Thermogram (top panel) for the calorimetric titration of $BoFPR_{ox}$ (10 µM) in calorimetric cell with $NADP^+$ (250 µM in syringe) at 25 °C and corresponding binding isotherm with ligand-normalized integrated heats (bottom panel). All experiments were performed in Tris/HCl 25 mM, pH 7.4.

We have then explored the ability of BoFPR to oxidize NADPH, by evaluating its diaphorase activity to transfer electrons from NADPH to the artificial electron acceptor DCPIP. Our data indicate an oxido-reductase activity that depends on the NADPH concentration with inhibition by its excess (Fig. 3A). Data fitting to the Michaelis-Menten equation that takes into account such inhibition (Eq. (2)) allows to determine k_{cat}, K_M^{NADPH} and K_i for BoFPR in the values of 14.3 ± 0.7 s^{-1}, 3.7 ± 0.2 µM, and 52 ± 8 µM, respectively. K_M^{NADPH} is in the range described for both FNRs and FPRs, while k_{cat}, following the trait of other FPRs, is considerably lower than that found in FNRs [56,58,59]. Such traits have been claimed as the causes for differences in catalytic efficiency so far described between FNRs and FPRs. Nonetheless, it is remarkable the strong deleterious effect of the NADPH excess on BoFPR activity, while in other family members considerably more modest deleterious effects are observed [60]. Finally, NADPH oxidation is not detected when using either molecular oxygen or

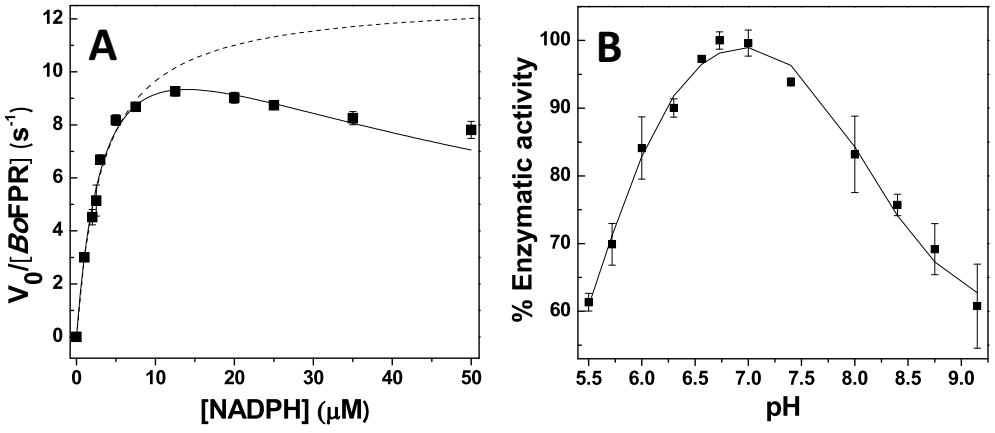

Fig. 3. Steady-state catalytic activity of BoFPR. (A) Steady-state kinetic profile for the diaphorase activity of BoFPR. Experimental data were fitted to the Michaelis-Menten equation when considering inhibition by excess of substrate (solid line) or in the absence of inhibition (dotted line). Measurements were recorded with 20 nM BoFPR in Tris/HCl 25 mM, pH 7.4, using 95 µM DCPIP and a 0–50 µM range of NADPH at 25 °C. (B) Effect of pH on the apparent rate constant at 12.5 µM NADPH as a function of pH. Line shows data fitting to Eq. (3).

superoxide as BoFPR electron acceptors, suggesting that the enzyme has neither oxidase nor superoxide reductase activities.

The BoFPR DCPIP diaphorase activity is highly dependent on the pH, with maximal activity at pH 6.7 and two inflection points at 5.5 ± 0.7 and 8.1 ± 0.1 (Fig. 3B). The first fits well with the theoretical isoelectric point of the protein sequence, pI ~5.6, indicating that the activity decrease when lowering the pH from 6.7 to 5.5 might relate to the enzyme change in charge. The second pK_a suggests a deprotonation at the active site over pH 8.0. Since in the structures below described no residue around the active site is predicted to have a pK_a close to 8, this protonation might be related to a change in the protonation state of the flavin isoalloxazine ring [61].

As the chemical compound 1-[5-(4-Chloro-benzylsulfanyl)-[1,3,4] thiadiazol-2-yl]-3-(4-chloro-phenyl)-urea (named D5) was recently shown as inhibitor of XacFPR [30], we have here evaluated also its potential, as well as that of four analogues (Table SP1), as BoFPR inhibitors. All five compounds show high IC_{50} values on the NADPH-dependent BoFPR diaphorase activity (160–1900 μM range) (Table SP1), and the more efficient one, D5, is only able to decrease the enzyme activity over 80% at IC_{max}. As a consequence, D5 appears species specific for XacFPR versus BoFPR, and none of the here studied compounds turns out to be good inhibitors of BoFPR.

3.3. Hydride transfer from NADPH to BoFPR is the reaction limiting step and occurs through formation of two charge transfer complexes between the donor and acceptor rings

We then used stopped-flow with photodiode array detection to evaluate the reductive half-reaction conducting to NADPH oxidation (Fig. 4). Anaerobic fast mixing of NADPH with $BoFPR_{ox}$ courses with fast stabilisation of a band centred in the 580–600 nm region compatible with the formation of a CTC between the oxidized isoalloxazine and the reduced nicotinamide rings, FPR_{ox}:NADPH, labelled before as CTC-1 in other FNRs and FPRs [32,33,58] (Fig. 4A). Stepwise formation

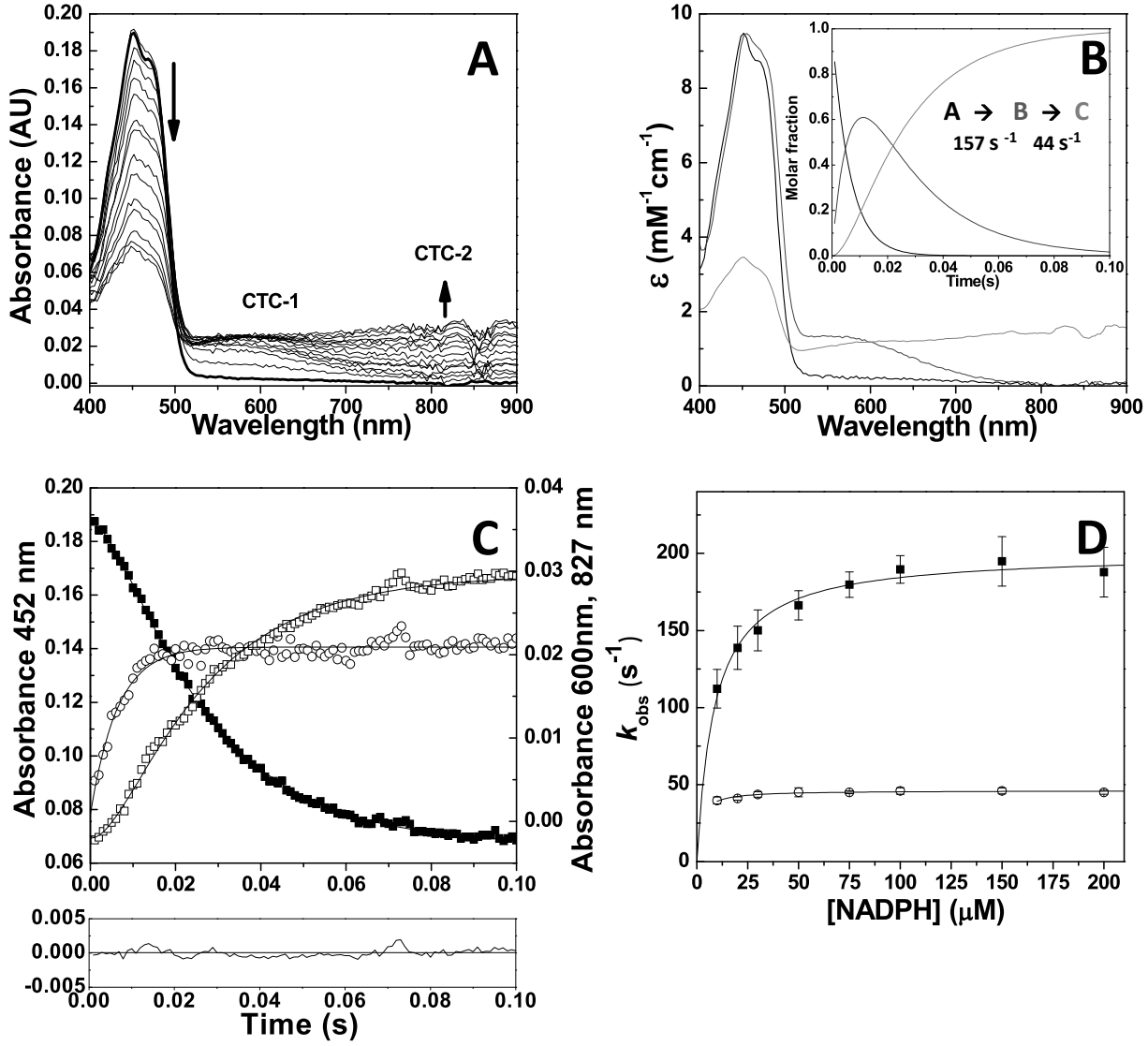

Fig. 4. Pre-steady-state activity of BoFPR. Kinetic evaluation of the NADPH oxidation by $BoFPR_{ox}$ as followed by stopped-flow spectrophotometry. (A) Spectral evolution for the mixing of BoFPR (20 μM) with NADPH (60 μM) in 25 mM Tris/HCl, pH 7.4, at 6 °C in a 100 ms timescale. The bold line represents the BoFPR spectrum before mixing. Formation of two CTCs at 580–600 nm (CTC-1) and 820–860 nm (CTC-2) are detected. (B) Spectral deconvolution of intermediate species observed during the reaction of $BoFPR_{ox}$ with NADPH when using a three states fitting model (A → B → C); species A, B and C are shown in black, dark grey and grey continuous lines, respectively. The inset shows their evolution profile. (C) Kinetic traces at 452 nm (closed squares), 600 nm (open circles) and 827 nm (open squares). The residual of the fit at 827 nm is shown at the bottom. (D) Dependence of $k_{A\rightarrow B}$ (closed squares) and $k_{B\rightarrow C}$ (open circles) on the NADPH concentration. Data fitting to Eq. (4) are presented.

of this band is detected in experiments at 6 °C, but this process becomes too fast at 25 °C to be detected (not shown). Subsequent spectroscopic changes bring about the decrease of the 452 nm flavin band-I, indicative of isoalloxazine reduction by hydride transfer (HT) from NADPH, and the appearance of a second broad charge transfer band centred around 840 nm that agrees with a FPR_{hq}:$NADP^+$ CTC species (CTC-2) (Fig. 4A). Global analysis of spectral evolution at 6 °C best fits to a three species model, A → B → C. The initial identified spectroscopic species (A) closely relates to $BoFPR_{ox}$. Features of the intermediate species (B) are suggestive of the binding of the NADPH substrate and the formation of a CTC-1 species. The final species (C) is mainly contributed by a CTC-2 spectrum, indicating that HT has already taken place (Fig. 4B–C). Thus, data at 6 °C allow estimation of observed conversion rate constants for NADPH binding and CTC-1 formation ($k_{A\rightarrow B}$), as well as those ($k_{B\rightarrow C}$) consistent with transformation of CTC-1 into CTC-2 that include the HT process. $k_{A\rightarrow B}$ values show a hyperbolical dependence on the NADPH concentration (Fig. 4D), allowing to determine a dissociation constant for NADPH binding to $BoFPR_{ox}$ ($K_d^{CTC\text{-}1}$) of 8.7 ± 0.9 μM and limiting rate for this CTC-1 formation of 200 ± 3 s^{-1}. On the contrary $k_{B\rightarrow C}$ values hardly showed concentration dependence in the over 1:1 protein:NADPH ratio assayed, suggesting that they nearly correspond to the limiting rate for the HT (k_{HT}), being in this case of 48 ± 1 s^{-1}. To the best of our knowledge this is the first report of parameters for CTC-1 and CTC-2 formation obtained independently for a FNR/FPR family member. In addition, these data identify the HT itself as the limiting step in the semi-reductive half reduction where BoFPR is reduced by NADPH. Moreover, when compared with the steady-state parameters they also envisage product release from the CTC-2 complex as limiting the overall BoFPR turnover. Nonetheless, in experiments at 25 °C, CTC-1 formation occurs within the instrumental dead-time and a single step mechanism applies, being this what was so far described for FNRs and FPRs [32,33]. At this temperature k_{obs} also depends hyperbolically on the NADPH concentration, but in this case it will account for NADPH binding, for reorganization of the Michaelis complex into the CTC-1 and for the HT process itself, allowing to determine a $^{app}K_d^{NADPH}$ of 31 ± 5 μM, and $^{app}k_{HT}$ of 167 ± 5 s^{-1}. These values are in the range of those reported for other FPRs, particularly of subclass I, while are consistently higher and lower respectively than those in FNRs [32,58]. In addition, BoFPR behaves similarly to other subclass I FPRs regarding spectroscopic stabilisation of CTC-1 and, particularly, of CTC-2 during catalysis, while only CTC-1 stabilisation has been reported for subclass II FPRs [32,58].

Therefore, in BoFPR, as in the other bacterial FPRs, formation of these CTCs during HT from NADPH is suggestive of stacking of the

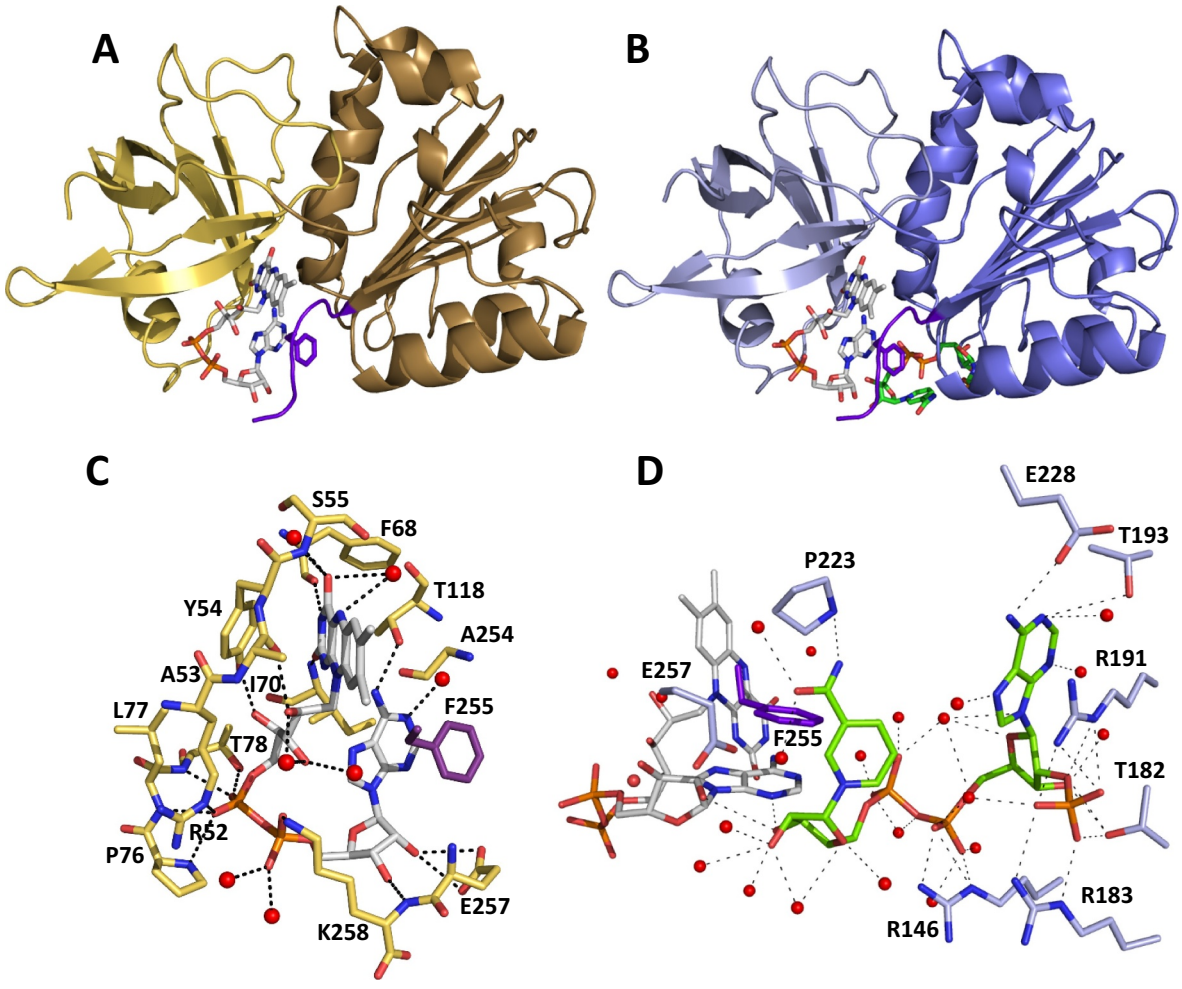

Fig. 5. Crystal structures for $BoFPR_{ox}$ and $BoFPR_{ox}$:$NADP^+$ complex. (A) Cartoon representation of $BoFPR_{ox}$ (PDB ID: 6RR3). N-terminal and C-terminal domains are shown in wheat and brown respectively. (B) Cartoon representation of $BoFPR_{ox}$:$NADP^+$ complex (PDB ID: 6RRA). N-terminal and C-terminal domains are shown in pale and dark blue respectively. In (A) and (B) the C-terminal tail is coloured in purple with the F255 side-chain (stacking the adenine of FAD) shown in sticks. (C) H-bond network stabilising the FAD folded conformation of BoFPR and detail of the stacking of F255 (violet) to its adenine. (D) H-bond network stabilising $NADP^+$ binding in the BoFPR:$NADP^+$ complex. Parallel- and T-stacking of F255 (violet) to the FAD adenine moiety and the nicotinamide of $NADP^+$ is observed. In (C) and (D) water molecules are represented as red spheres. In all panels FAD is shown in sticks with carbon atoms in white, while in (B) and (D) $NADP^+$ is in sticks with green carbon atoms.

reactive isoalloxazine and nicotinamide rings to encounter their respective N5 and C4 atoms to allow direct HT, as also proposed in FNRs [16,32,62]. Differences in the side-chain stacking against the isoalloxazine suggest dissimilarities in competent active site geometries within FPR subclasses, where it is suggested that the initial pre-organization of CTC-1 situates the N5 of FAD and the C4 of NADPH reacting atoms at optimal tunnel distance in a stiff competent active site [32]. In addition, the C-terminal tail in FPRs suggests an overall more complex mechanism than in FNRs. Thus, the higher reorganization energy to attain the catalytically competent state and the minimization of gating contribution in tunnelling ready conformations in FPRs makes them less efficient in the HT processes than FNRs [32,63].

3.4. Crystal structures of B. ovis FPR$_{ox}$ do not envisage the coupling of reactant rings

To evaluate coupling of BoFPR$_{ox}$ and the coenzyme at the atomic level, we have solved the 3D structure of BoFPR$_{ox}$ in the absence (Fig. 5A) and presence of NADP$^+$ (Fig. 5B). BoFPR$_{ox}$ consist of an N-terminal domain (residues 3–98) that folds into a six-stranded antiparallel β-barrel and a short α-helix, and of a C-terminal domain (residues 99–258) built of a Rossmann nucleotide binding fold (Fig. 5A). Such overall folding resembles those of other bacterial FPRs, as the subtype Ia from *Xanthomonas citri* subsp. *citri* (XacFPR), the subtype Ib from *Rhodobacter capsulatus* (RcFPR) and the subtype II from *Escherichia coli* (EcFPR) (Table SP3). As other FPRs, BoFPR lacks of the large FAD-binding domain loop that interacts with the adenylate moiety of the cofactor in plastidic FNRs. This is one of the reasons why its FAD adopts a folded conformation (Fig. 5A) [15,58]. Folded FAD is stabilised by the stacking of the adenine ring to Phe255 at the C-terminal tail (Fig. 5C), while the adenine ribose interacts with the C-terminal Glu257 and Lys258. Arg52, Pro76, Leu77, Thr78 and Lys258 H-bond the FAD pyrophosphate, while Tyr54 and Ile70 H-bond the flavin ribityl chain (Fig. 5C). Ser55, Ile70 and Phe68 H-bond the isoalloxazine, and Tyr54 and Ala254 respectively stack at its *Si*- and *Re*-face. Seven water molecules complete this H-bonds network. The Ala at the *Re*-face of the isoalloxazine and the residue properties at the C-terminal sequence (Fig. SP1) fit BoFPR$_{ox}$ in the subclass Ia. As expected, BoFPR also conserves, in sequence and spatial conformation (Figs. SP1 and SP2), the catalytic triad (S55, C220 and E252 in BoFPR) directly involved in the interaction with the NADP$^+$ nicotinamide ring in the FNR family [1].

The BoFPR$_{ox}$:NADP$^+$ structure keeps the overall protein folding and active site features, showing very minor changes to accommodate NADP$^+$ (RMSD 0.23 Å for 229 Cα) (Fig. 5B). NADP$^+$ binds through its 2′P-AMP moiety while its redox reactive nicotinamide nucleotide (NMN) moiety orients out of the active site and barely interacts with the protein (Fig. 5D), as so far reported in all experimental FPR and FNR structures in complex with NADP$^+$ [44,55,64–66]. Binding of the 2′P-AMP moiety displaces Arg146 and Arg191 side-chains (by ~4.5 Å) and reduces their mobility (Fig. SP2A and B). Arg146 contributes to the NADP$^+$ pyrophosphate binding, Arg191, Thr182 and Arg183 stabilise the ribose 2′-P charge, and Thr193 and Glu228 the adenine base. On the contrary, the NMN moiety is largely accessible to the solvent, with one of the nicotinamide ring sides in front of Pro223 and the C-tail residues Phe255 and Glu257. Interestingly, soaking of NADP$^+$ does not influence the Phe255 position that maintains its stacking to the adenine of FAD and favours T-stacking of the nicotinamide ring against them (Fig. 5D). B-factor values of FAD in BoFPR$_{ox}$ envisage some flexibility for the ribose and the pyrophosphate cofactor moieties facing the solvent, while FAD overall decreases in BoFPR$_{ox}$:NADP$^+$ (Fig. SP2C and D).

Therefore, the nicotinamide conformation observed in our BoFPR$_{ox}$:NADP$^+$ structure is far from envisaging the competent flavin-nicotinamide coupling for catalysis foreseen by our kinetic studies. Nonetheless, our structural observations agree with the in solution structural data that indicate no coupling of rings when, as in this case, both are in the oxidized state.

3.5. Thermal effects on molecular simulations allow to envisage formation of a catalytic competent organization

According to the formation of CTCs during HT, we would expect that displacement of the adenine moiety of FAD and of the C-terminal tail of bacterial FPRs would contribute to coupling of reacting flavin and nicotinamide rings. As there are not experimental data supporting a nicotinamide active site entrance path, we have here used a MD approach to simulate a potential BoFPR$_{ox}$:NADPH catalytically competent complex architecture. Our initial MD simulations at 27 °C show slightly faster stabilisation of the BoFPR$_{ox}$:NADPH model than that of the BoFPR$_{ox}$, with the complex exhibiting lower RMSD values and both maintaining overall crystallographic folding (Figs. SP3 and SP4). Root mean square fluctuations (RMSF) indicate that the FAD keeps position along simulation time, nonetheless, its adenine nucleotide moiety results much more flexible than its isoalloxazine moiety (Fig. SP3B). In the BoFPR$_{ox}$:NADPH model, RMSFs suggest stable coupling of the 2′P-AMP moiety of the NADPH, while its NMN moiety is more flexible, solvent exposed and hardly in contact with the protein chain. RMSFs for BoFPR$_{ox}$ and BoFPR$_{ox}$:NADPH Cα atoms agree with the protein core around the active site having very low flexibility (Fig. SP3B). Therefore, these simulations indicate a packed isoalloxazine environment and do not envisage access of the nicotinamide ring to the FPR active site, in agreement with crystal structures and biochemical characterizations in other FPRs [44,55,58].

In this context, production of a HT competent conformation bringing together the flavin and nicotinamide rings can be considered as an infrequent event that might be explored by applying a Temperature Accelerated MD method [67]. We have run short MD simulations of the BoFPR$_{ox}$:NADPH model at increasing temperatures (Fig. SP5). RMSD and radius of gyration at 150 °C suggest protein unfolding, while at 100 °C uncoupling of NADPH is observed. No changes in these parameters are however detected at lower temperatures. Longer MD simulations at 50 °C show a stable complex, with low RMSD and a nearly constant isoalloxazine interaction network (Fig. SP6). Nonetheless, some fluctuations in the radius of gyration are observed, and in some replicas the FAD transiently populates an extended conformation where its adenine moiety opens towards the solvent (maximum isoalloxazine:adenine distance at 8.2 ns in Fig. 6A) as a consequence of the C-terminal tail displacement and uncoupling the adenine:F255 stacking. Such displacement allows approaching of the NADPH nicotinamide ring towards the active site, decreasing the distance between the N5 and C4 reacting atoms up to 8 Å (Fig. SP6B). It is worth to note that our approach treating the transient displacement towards the solvent of the adenine of FAD as an infrequent event assisted by the C-terminal tail, agrees with experimental data on shortened RcFPR variants which despite leaving FAD in a more exposed situation do not promote significant changes in its folded conformation [58].

We then selected one of the snapshots showing the FAD extended conformation and the shorted reacting atoms distance (8.2 ns in Fig. 6A) as starting structure of longer MDs at physiological temperature (37 °C). The new simulations show transient snapshots characterized by N5-C4 distances which might be short enough (up to only 4.8 Å) for a direct HT (Fig. 6B). In these snapshots fully parallel stacking of the isoalloxazine and nicotinamide reacting rings is prevented by the adenine ring of FAD, particularly by its amide group, that keeps the corresponding N10-C2 distances larger than the N5-C4 ones (Fig. 6B).

3.6. The adenine moiety of FAD in FPRs might mimic the C-terminal aromatic in FNRs during HT catalysis

Mutational and theoretical analysis to the C-terminal Tyr residue

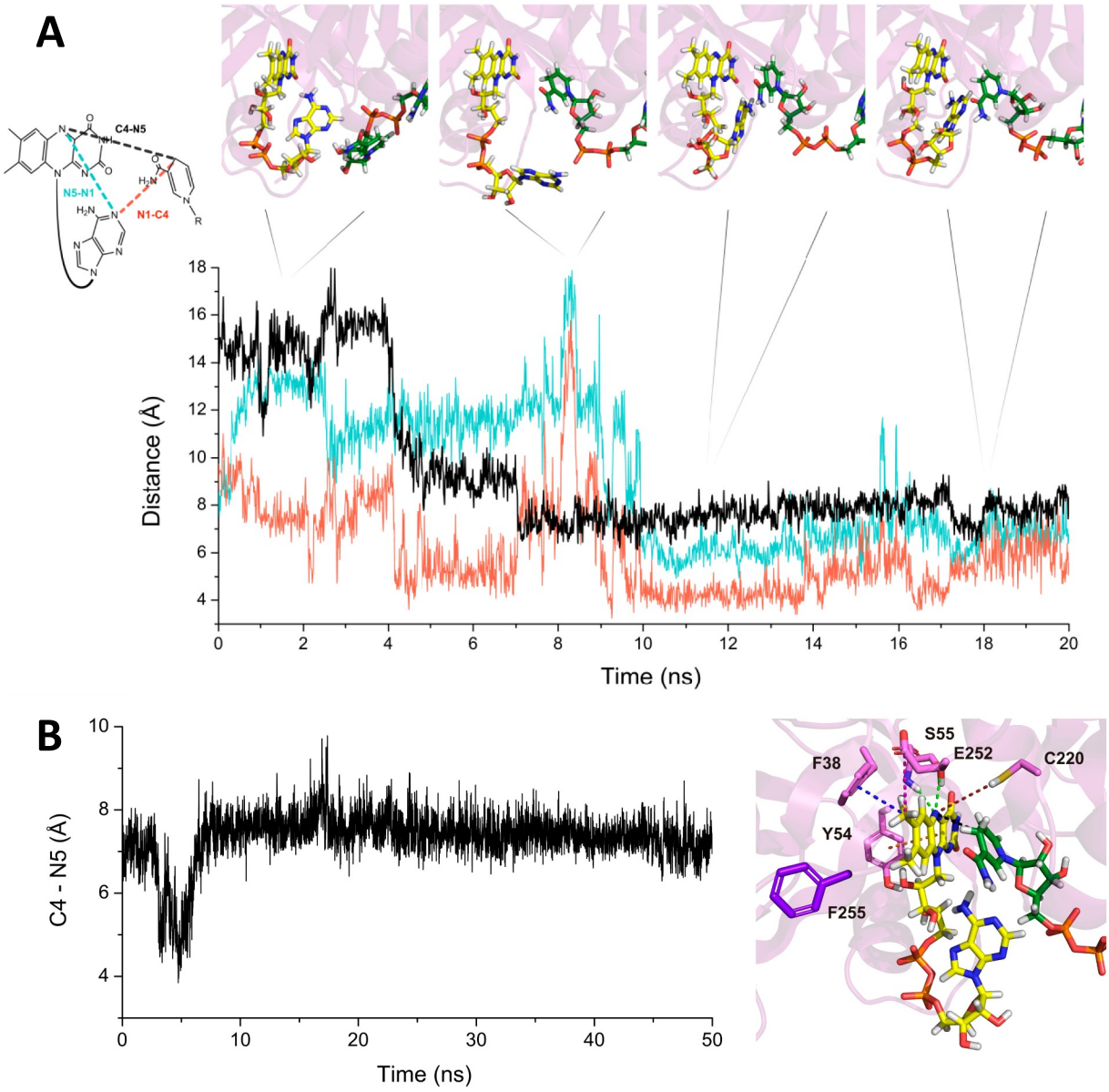

Fig. 6. Simulation of the coupling of the FAD and NADPH redox active rings. (A) Time evolution of the relative position of the nicotinamide of NADPH regarding the isoalloxazine and adenine moieties of the FAD in a temperature accelerated MD run at 50 °C for the $BoFPR_{ox}$:NADPH complex. Figure shows evolution of distances from the reactive C4 atom of the nicotinamide regarding two FAD positions, N5 isoalloxazine and N1 adenine, as well as between these two FAD positions. Top panels show relative dispositions of FAD (carbons in yellow) and NADPH (carbons in green) in representative frames at 2, 8.2, 10.5 and 18.5 ns of the MD simulation. (B) Time evolution of the reactant atoms distance (C4 nicotinamide and N5 FAD) along a MD simulation at 37 °C when using as starting structure the snapshot than minimizes such distance whereas maximizing distances to the N1 adenine in the temperature accelerated MD simulation (8.2 ns structure in the 50 °C MD). On the right it is shown the structural model for the snapshot (4.74 ns) showing the minimum distance, with FAD, NADPH and some active site residues shown in sticks (colour code as in A, and as in SP5B for lines).

stacking at the *Re*-face of the isoalloxazine ring in plastidic FNRs pointed to this residue having a critical role in HT between the N5 of the FAD(H^-) and the C4 of the nicotinamide ring of $NADP^+$(H). Though the presence of this Tyr was not obligatory for HT, it was shown to be crucial for the high catalytic efficiency of FNRs by i) modulating the FAD midpoint reduction potential, ii) avoiding a too strong interaction between the reacting rings that would be incompatible with product release, iii) contributing to the optimal geometry between the N5 and C4 reacting atoms for HT, and iv) providing flexibility at the active site for the HT step to occur through tunnelling [16,17,68,69]. FPRs have a short C-terminal tail, 1 to 6 residues long, beyond the residue in front of the isoalloxazine *Re*-face. Moreover, in subclass I this residue is not aromatic anymore and it is usually replaced by an Ala (Fig. SP1). Thus, in FPRs the C-terminal tail together with the adenosine moiety of the folded FAD occludes access of the nicotinamide to the active site (Fig. 5B and D) [44,55]. So far, we have no structural details about a potential arrangement for the coupling of reacting rings in FPRs, but CTC formation during catalysis is reported in several species [32], including BoFPR (Fig. 4), pointing to their stacking. Contrary to that observed in plastidic FNRs (where $NADP^+$/H binding at the 2′P-AMP has a key impact in the relative disposition of the reacting rings), structural, binding and dynamic kinetic studies point to low contributions of NADPH binding at the 2′P-AMP site to attain the catalytic complex in FPRs. Instead, these studies suggest fluctuations at the C-terminal tail as potential promotors to increase the probability of competent nicotinamide:isoalloxazine couplings [32,44,55,70,71]. In addition, while pre-organization motions to accommodate the NADPH in the active site, including active site compression, favour overall

catalytic enhancement in FNRs, those effects have been shown to contribute much less to catalysis in FPRs [32,66,72].

Our simulations suggest that, facilitated by the C-terminal tail dynamics, the adenine moiety of the BoFPR FAD can transiently move towards the solvent, moment in which the nicotinamide of the NADPH can make its way towards the active site (Figs. 6 and SP6). The data also suggest that the direct and parallel stacking of the nicotinamide ring to the isoalloxazine ring is avoided by the adenine moiety of FAD (Fig. 6B). Noticeably, such snapshots of the dynamics resemble the competent catalytic conformation suggested for plastidic FNRs during catalysis, where it is the key C-terminal Tyr residue above mentioned the one avoiding parallel stacking of reacting rings [17,62]. This will suggest that in subclass I FPRs, the adenine of FAD will contribute to attain an optimal geometry during catalysis that avoids a strong interaction between the reacting rings. On its side, the C-terminal tail, despite not being directly involved in the catalytic event, will rather modulate the strength of molecular links to expedite the entry and exit of $NADP^+$/H.

In conclusion, BoFPR is a bacterial subclass I FPR that oxidizes NADPH through the formation of two CTCs, occurring before and after the HT event. Therefore, during catalysis binding of NADPH takes place with stacking of the nicotinamide and flavin reacting rings. However, as reported for other FPRs, x-ray diffraction, at least from $BoFPR_{ox}$:$NADP^+$ crystals generated in aerobic conditions, does not allow envisaging neither a catalytic competent geometry nor how it is attained. The use of all-atom MD simulations with a thermal effect approach allows producing potential competent isoalloxazine:nicotinamide interactions envisage a potential role to facilitate catalysis for the folded FAD in FPRs. In the BoFPR models the FAD folded conformation places its adenine moiety among the reacting rings, suggesting that during catalysis the adenine of FAD might have some of the roles claimed for the C-terminal Tyr in the plastidic family members.

Transparency document

The Transparency document associated with this article can be found, in online version.

Declaration of competing interest

No competing financial interests exist.

Acknowledgements

This work has been supported by the Spanish Ministry of Economy, Industry and Competitiveness (MINECO) [BIO2016-75183-P AEI/FEDER, UE to M.M.], and the Gobierno de Aragón-FEDER [Grupo de Referencia Biología Estructural (E35_17R to M.M.)]. The authors acknowledge Diamond Light Source and ALBA synchrotrons for beamtimes (proposal mx14739 and 2018072896, respectively), and their staff of beamlines I24 (DLS) and BL13 (XALOC) for assistance. Authors would like to acknowledge the use of Servicio General de Apoyo a la Investigación-SAI, Universidad de Zaragoza.

Authors' contributions

M.M.-J. and M.M., conceptualization, funding acquisition, project administration, supervision, writing-review and editing. D.P.-A., V.-T., S.B., E.A.-C, M.S., A.V.-C., and V.P., investigation, formal analysis, writing-original draft.

Appendix A. Supplementary data

Supplementary data to this article can be found online at https://doi.org/10.1016/j.bbabio.2019.148058.

References

[1] A. Aliverti, V. Pandini, A. Pennati, M. de Rosa, G. Zanetti, Structural and functional diversity of ferredoxin-NADP+ reductases, Arch. Biochem. Biophys. 474 (2008) 283–291.
[2] E.A. Ceccarelli, A.K. Arakaki, N. Cortez, N. Carrillo, Functional plasticity and catalytic efficiency in plant and bacterial ferredoxin-NADP(H) reductases, Biochim. Biophys. Acta 1698 (2004) 155–165.
[3] P. Mulo, M. Medina, Interaction and electron transfer between ferredoxin-NADP (+) oxidoreductase and its partners: structural, functional, and physiological implications, Photosynth. Res. 134 (2017) 265–280.
[4] G. Hanke, P. Mulo, Plant type ferredoxins and ferredoxin-dependent metabolism, Plant Cell Environ. 36 (2013) 1071–1084.
[5] A.S. López Rivero, M.A. Rossi, E.A. Ceccarelli, D.L. Catalano-Dupuy, A bacterial 2[4Fe4S] ferredoxin as redox partner of the plastidic-type ferredoxin-NADP, Biochim. Biophys. Acta Gen. Subj. 1863 (2019,) 651–660.
[6] X. Guan, S. Chen, C.P. Voon, K.B. Wong, M. Tikkanen, B.L. Lim, FdC1 and leaf-type ferredoxins channel electrons from photosystem I to different downstream electron acceptors, Front. Plant Sci. 9 (2018) 410.
[7] C. Bittel, L.C. Tabares, M. Armesto, N. Carrillo, N. Cortez, The oxidant-responsive diaphorase of Rhodobacter capsulatus is a ferredoxin (flavodoxin)-NADP(H) reductase, FEBS Lett. 553 (2003) 408–412.
[8] P.J. Pomposiello, B. Demple, Identification of SoxS-regulated genes in Salmonella enterica serovar typhimurium, J. Bacteriol. 182 (2000) 23–29.
[9] M.L. Tondo, M.A. Musumeci, M.L. Delprato, E.A. Ceccarelli, E.G. Orellano, Structural-functional characterization and physiological significance of ferredoxin-NADP+ reductase from Xanthomonas axonopodis pv. citri, PLoS One 6 (2011) e27124.
[10] A.R. Krapp, R.E. Rodriguez, H.O. Poli, D.H. Paladini, J.F. Palatnik, N. Carrillo, The flavoenzyme ferredoxin (flavodoxin)-NADP(H) reductase modulates NADP(H) homeostasis during the soxRS response of Escherichia coli, J. Bacteriol. 184 (2002) 1474–1480.
[11] P.J. Pomposiello, M.H. Bennik, B. Demple, Genome-wide transcriptional profiling of the Escherichia coli responses to superoxide stress and sodium salicylate, J. Bacteriol. 183 (2001) 3890–3902.
[12] J.L. Brumaghim, Y. Li, E. Henle, S. Linn, Effects of hydrogen peroxide upon nicotinamide nucleotide metabolism in Escherichia coli: changes in enzyme levels and nicotinamide nucleotide pools and studies of the oxidation of NAD(P)H by Fe(III), J. Biol. Chem. 278 (2003) 42495–42504.
[13] E. Sevilla, M.T. Bes, A. González, M.L. Peleato, M.F. Fillat, Redox-based transcriptional regulation in prokaryotes: revisiting model mechanisms, Antioxid. Redox Signal. 30 (2019) 1651–1696.
[14] A.R. Krapp, M.V. Humbert, N. Carrillo, The soxRS response of Escherichia coli can be induced in the absence of oxidative stress and oxygen by modulation of NADPH content, Microbiology. 157 (2011) 957–965.
[15] L. Serre, F.M. Vellieux, M. Medina, C. Gómez-Moreno, J.C. Fontecilla-Camps, M. Frey, X-ray structure of the ferredoxin:NADP+ reductase from the cyanobacterium Anabaena PCC 7119 at 1.8 Å resolution, and crystallographic studies of NADP+ binding at 2.25 Å resolution, J. Mol. Biol. 263 (1996) 20–39.
[16] I. Lans, M. Medina, E. Rosta, G. Hummer, M. Garcia-Viloca, J.M. Lluch, et al., Theoretical study of the mechanism of the hydride transfer between ferredoxin-NADP+ reductase and NADP+: the role of Tyr303, J. Am. Chem. Soc. 134 (2012) 20544–20553.
[17] I. Lans, J.R. Peregrina, M. Medina, M. García-Viloca, A. González-Lafont, J.M. Lluch, Mechanism of the hydride transfer between Anabaena Tyr303Ser FNRrd/FNRox and NADP+/H. A combined pre-steady-state kinetic/ensemble-averaged transition-state theory with multidimensional tunneling study, J. Phys. Chem. B 114 (2010) 3368–3379.
[18] D.H. Paladini, M.A. Musumeci, N. Carrillo, E.A. Ceccarelli, Induced fit and equilibrium dynamics for high catalytic efficiency in ferredoxin-NADP(H) reductases, Biochemistry. 48 (2009) 5760–5768.
[19] X. Liu, M. Zhou, Y. Yang, J. Wu, Q. Peng, Overexpression of Cu-Zn SOD in *Brucella abortus* suppresses bacterial intracellular replication via down-regulation of Sar1 activity, Oncotarget. 9 (2018) 9596–9607.
[20] J.O. Korbel, L.J. Jensen, C. von Mering, P. Bork, Analysis of genomic context: prediction of functional associations from conserved bidirectionally transcribed gene pairs, Nat. Biotechnol. 22 (2004) 911–917.
[21] A.L. Ridler, D.M. West, Control of Brucella ovis infection in sheep, Vet. Clin. North Am. Food Anim. Pract. 27 (2011) 61–66.
[22] N. Picard-Hagen, X. Berthelot, J.L. Champion, L. Eon, F. Lyazrhi, M. Marois, et al., Contagious epididymitis due to Brucella ovis: relationship between sexual function, serology and bacterial shedding in semen, BMC Vet. Res. 11 (2015) 125.
[23] F. De Massis, K. Zilli, G. Di Donato, R. Nuvoloni, S. Pelini, L. Sacchini, et al., Distribution of Brucella field strains isolated from livestock, wildlife populations, and humans in Italy from 2007 to 2015, PLoS One 14 (2019) e0213689.
[24] J. Lykkesfeldt, O. Svendsen, Oxidants and antioxidants in disease: oxidative stress in farm animals, Vet. J. 173 (2007) 502–511.
[25] P. Macheroux, UV–visible spectroscopy as a tool to study flavoproteins, Methods Mol. Biol. 131 (1999) 1–7.
[26] S. Frago, I. Lans, J.A. Navarro, M. Hervás, D.E. Edmondson, M.A. De la Rosa, et al., Dual role of FMN in flavodoxin function: electron transfer cofactor and modulation of the protein-protein interaction surface, Biochim. Biophys. Acta 2010 (1797) 262–271.
[27] M. Martínez-Júlvez, M. Medina, A. Velázquez-Campoy, Binding thermodynamics of ferredoxin:NADP+ reductase: two different protein substrates and one energetics,

Biophys. J. 96 (2009) 4966–4975.
[28] A. Velázquez-Campoy, G. Goñi, J.R. Peregrina, M. Medina, Exact analysis of heterotropic interactions in proteins: characterization of cooperative ligand binding by isothermal titration calorimetry, Biophys. J. 91 (2006) 1887–1904.
[29] J. Sancho, The stability of 2-state, 3-state and more-state proteins from simple spectroscopic techniques… plus the structure of the equilibrium intermediates at the same time, Arch. Biochem. Biophys. 531 (2013) 4–13.
[30] M. Martínez-Júlvez, G. Goñi, D. Pérez-Amigot, R. Laplaza, I.A. Ionescu, S. Petrocelli, et al., Identification of inhibitors targeting ferredoxin-NADP$^+$ reductase from the Xanthomonas citri subsp. citri phytopathogenic bacteria, Molecules. 23 (2017).
[31] P. Ferreira, M. Medina, F. Guillen, M. Martinez, W. Van Berkel, A. Martinez, Spectral and catalytic properties of aryl-alcohol oxidase, a fungal flavoenzyme acting on polyunsaturated alcohols, Biochem. J. 389 (2005) 731–738.
[32] A. Sánchez-Azqueta, D.L. Catalano-Dupuy, A. López-Rivero, M.L. Tondo, E.G. Orellano, E.A. Ceccarelli, et al., Dynamics of the active site architecture in plant-type Ferredoxin-NADP(+) reductases catalytic complexes, Biochim. Biophys. Acta 1837 (2014) 1730–1738.
[33] J. Tejero, J.R. Peregrina, M. Martínez-Júlvez, A. Gutiérrez, C. Gómez-Moreno, N.S. Scrutton, et al., Catalytic mechanism of hydride transfer between NADP+/H and ferredoxin-NADP+ reductase from Anabaena PCC 7119, Arch. Biochem. Biophys. 459 (2007) 79–90.
[34] W. Kabsch, Xds. Acta Crystallogr. D Biol. Crystallogr. 66 (2010) 125–132.
[35] P. Evans, Scaling and assessment of data quality, Acta Crystallogr. D Biol. Crystallogr. 62 (2006) 72–82.
[36] M.D. Winn, C.C. Ballard, K.D. Cowtan, E.J. Dodson, P. Emsley, P.R. Evans, et al., Overview of the CCP4 suite and current developments, Acta Crystallogr. D Biol. Crystallogr. 67 (2011) 235–242.
[37] A. Vagin, A. Teplyakov, MOLREP: an automated program for molecular replacement, J. Appl. Crystallogr. 30 (1997) 1022–1025.
[38] G.N. Murshudov, A.A. Vagin, E.J. Dodson, Refinement of macromolecular structures by the maximum-likelihood method, Acta Crystallogr. D Biol. Crystallogr. 53 (1997) 240–255.
[39] P. Emsley, B. Lohkamp, W.G. Scott, K. Cowtan, Features and development of Coot, Acta Crystallogr. D Biol. Crystallogr. 66 (2010) 486–501.
[40] R.A. Laskowski, M.W. MacArthur, D.S. Moss, J.M. Thornton, PROCHECK: a program to check the stereochemical quality of protein structures, J. Appl. Crystallogr. 26 (1993) 283–291.
[41] G. Sridhar Prasad, N. Kresge, A.B. Muhlberg, A. Shaw, Y.S. Jung, B.K. Burgess, et al., The crystal structure of NADPH:ferredoxin reductase from Azotobacter vinelandii, Protein Sci. 7 (1998) 2541–2549.
[42] M.P. Jacobson, D.L. Pincus, C.S. Rapp, T.J. Day, B. Honig, D.E. Shaw, et al., A hierarchical approach to all-atom protein loop prediction, Proteins. 55 (2004) 351–367.
[43] Schrödinger. Schrödinger Release 2017-1. New York, NY.: Schrödinger LLC; 2017.
[44] A. Wang, J.C. Rodríguez, H. Han, E. Schönbrunn, M. Rivera, X-ray crystallographic and solution state nuclear magnetic resonance spectroscopic investigations of NADP + binding to ferredoxin NADP reductase from Pseudomonas aeruginosa, Biochemistry. 47 (2008) 8080–8093.
[45] Delano WL. The PyMOL molecular graphics system. DeLano Scientific, San Carlos, CA, USA. 2002:http://www.pymol.org.
[46] Abraham MJ, Murtola T, Schulz R, Páll S, Smith JC, Hess B, et al. GROMACS: high performance molecular simulations through multi-level parallelism from laptops to supercomputers. SoftwareX. 2015;1–2:19–25.
[47] Y. Duan, C. Wu, S. Chowdhury, M.C. Lee, G. Xiong, W. Zhang, et al., A point-charge force field for molecular mechanics simulations of proteins based on condensed-phase quantum mechanical calculations, J. Comput. Chem. 24 (2003) 1999–2012.
[48] J. Wang, R.M. Wolf, J.W. Caldwell, P.A. Kollman, D.A. Case, Development and testing of a general amber force field, J. Comput. Chem. 25 (2004) 1157–1174.
[49] Frisch MJ, Trucks GW, H., Schlegel B, G. E. Scuseria, M. A. Robb, et al. Gaussian 09, Revision D.01. Wallingford CT: Gaussian, Inc.; 2016.
[50] J. Wang, W. Wang, P.A. Kollman, D.A. Case, Automatic atom type and bond type perception in molecular mechanical calculations, J. Mol. Graph. Model. 25 (2006) 247–260.
[51] Sousa da Silva AW, Vranken WF. ACPYPE - AnteChamber PYthon Parser interfacE. BMC Res Notes. 2012;5:367.
[52] W. Humphrey, A. Dalke, K. Schulten, VMD: visual molecular dynamics, J. Mol. Graph. 14 (1996) 33–38 (27-8).
[53] M.H.M. Olsson, C.R. Søndergaard, M. Rostkowski, J.H. Jensen, PROPKA3: consistent treatment of internal and surface residues in empirical pKa predictions, J. Chem. Theory Comput. 7 (2011) 525–537.
[54] A. Sánchez-Azqueta, B. Herguedas, R. Hurtado-Guerrero, M. Hervás, J.A. Navarro, M. Martínez-Júlvez, et al., A hydrogen bond network in the active site of Anabaena ferredoxin-NADP(+) reductase modulates its catalytic efficiency, Biochim. Biophys. Acta 2014 (1837) 251–263.
[55] A. Bortolotti, I. Pérez-Dorado, G. Goñi, M. Medina, J.A. Hermoso, N. Carrillo, et al., Coenzyme binding and hydride transfer in Rhodobacter capsulatus ferredoxin/flavodoxin NADP(H) oxidoreductase, Biochim. Biophys. Acta 2009 (1794) 199–210.
[56] M. Medina, M. Martínez-Júlvez, J.K. Hurley, G. Tollin, C. Gómez-Moreno, Involvement of glutamic acid 301 in the catalytic mechanism of ferredoxin-NADP+ reductase from Anabaena PCC 7119, Biochemistry. 37 (1998) 2715–2728.
[57] M.M. Koskela, K.M. Dahlström, G. Goñi, N. Lehtimäki, M. Nurmi, A. Velazquez-Campoy, et al., Arabidopsis FNRL protein is an NADPH-dependent chloroplast oxidoreductase resembling bacterial ferredoxin-NADP, Physiol. Plant. 162 (2018) 177–190.
[58] A. Bortolotti, A. Sánchez-Azqueta, C.M. Maya, A. Velázquez-Campoy, J.A. Hermoso, M. Medina, et al., The C-terminal extension of bacterial flavodoxin-reductases: involvement in the hydride transfer mechanism from the coenzyme, Biochim. Biophys. Acta 2014 (1837) 33–43.
[59] M. Martínez-Júlvez, G. Goñi, D. Pérez-Amigot, R. Laplaza, I.A. Ionescu, S. Petrocelli, et al., Identification of inhibitors targeting ferredoxin-NADP$^+$ reductase from the Xanthomonas citri subsp. citri phytopathogenic bacteria, Molecules. 23 (2018) 29.
[60] N. Carrillo, E.A. Ceccarelli, Open questions in ferredoxin-NADP+ reductase catalytic mechanism, Eur. J. Biochem. 270 (2003) 1900–1915.
[61] F. Müller, Free flavins: synthesis, chemical and physical properties, in: F. Müller (Ed.), Chemistry and Biochemistry of Flavoenzymes: Boca Raton, CRC Press, Fl, 1991, pp. 1–71.
[62] J.R. Peregrina, I. Lans, M. Medina, The transient catalytically competent coenzyme allocation into the active site of Anabaena ferredoxin NADP+-reductase, Eur. Biophys. J. 41 (2012) 117–128.
[63] C.R. Pudney, A. Guerriero, N.J. Baxter, L.O. Johannissen, J.P. Waltho, S. Hay, et al., Fast protein motions are coupled to enzyme H-transfer reactions, J. Am. Chem. Soc. 135 (2013) 2512–2517.
[64] M.A. Musumeci, H. Botti, A. Buschiazzo, E.A. Ceccarelli, Swapping FAD binding motifs between plastidic and bacterial ferredoxin-NADP(H) reductases, Biochemistry. 50 (2011) 2111–2122.
[65] A.S. Nascimento, D.L. Catalano-Dupuy, A. Bernardes, O. Neto Mde, M.A. Santos, E.A. Ceccarelli, et al., Crystal structures of Leptospira interrogans FAD-containing ferredoxin-NADP+ reductase and its complex with NADP+, BMC Struct. Biol. 7 (2007) 69.
[66] J.A. Hermoso, T. Mayoral, M. Faro, C. Gomez-Moreno, J. Sanz-Aparicio, M. Medina, Mechanism of coenzyme recognition and binding revealed by crystal structure analysis of ferredoxin-NADP+ reductase complexed with NADP+, J. Mol. Biol. 319 (2002) 1133–1142.
[67] M.R. Sorensen, A.F. Voter, Temperature-accelerated dynamics for simulation of infrequent events, J. Chem. Phys. 112 (2000) 9599–9606.
[68] J. Tejero, I. Pérez-Dorado, C. Maya, M. Martínez-Júlvez, J. Sanz-Aparicio, C. Gómez-Moreno, et al., C-terminal tyrosine of ferredoxin-NADP+ reductase in hydride transfer processes with NAD(P)+/H, Biochemistry. 44 (2005) 13477–13490.
[69] L. Piubelli, A. Aliverti, A.K. Arakaki, N. Carrillo, E.A. Ceccarelli, P.A. Karplus, et al., Competition between C-terminal tyrosine and nicotinamide modulates pyridine nucleotide affinity and specificity in plant ferredoxin-NADP+ reductase, J. Biol. Chem. 275 (2000) 10472–10476.
[70] I. Nogués, I. Pérez-Dorado, S. Frago, C. Bittel, S.G. Mayhew, C. Gómez-Moreno, et al., The ferredoxin-NADP(H) reductase from Rhodobacter capsulatus: molecular structure and catalytic mechanism, Biochemistry. 44 (2005) 11730–11740.
[71] J.T. Wan, J.T. Jarrett, Electron acceptor specificity of ferredoxin (flavodoxin):NADP + oxidoreductase from Escherichia coli, Arch. Biochem. Biophys. 406 (2002) 116–126.
[72] K.M. Kean, R.A. Carpenter, V. Pandini, G. Zanetti, A.R. Hall, R. Faber, et al., High-resolution studies of hydride transfer in the ferredoxin:NADP, FEBS J. 284 (2017) 3302–3319.